


High-impedance superconducting resonators and on-chip filters for circuit quantum electrodynamics with semiconductor quantum dots

X. Zhang¹, Z. Zhu,¹ N.P. Ong¹, and J.R. Petta^{2,3,*}

¹*Department of Physics, Princeton University, Princeton, New Jersey 08544, USA*

²*Department of Physics and Astronomy, University of California—Los Angeles, Los Angeles, California 90095, USA*

³*Center for Quantum Science and Engineering, University of California—Los Angeles, Los Angeles, California 90095, USA*

 (Received 4 July 2023; revised 26 November 2023; accepted 22 December 2023; published 11 January 2024)

Spin-photon coupling presents an enticing opportunity for the long-range coupling of spin qubits. The spin-photon coupling rate, g_s , is proportional to the charge-photon coupling rate, g_c . To move deeper into the strong-coupling regime, g_c can be enhanced by fabricating high-impedance cavities using high-kinetic-inductance films. Here, we report dc transport and microwave response investigations of niobium nitride (NbN) films of different thicknesses. The kinetic inductance increases rapidly as the film thickness is reduced below 50 nm and for 15-nm NbN films we measure a sheet kinetic inductance $L_{k,S} = 41.2$ pH/□. As an application of the high-kinetic-inductance films, we fabricate compact LC filters that are commonly used to reduce microwave leakage in circuit quantum electrodynamics (cQED) devices. These filters feature up to 60 dB of attenuation near typical cavity resonance frequencies of $f_c = 8$ GHz.

DOI: [10.1103/PhysRevApplied.21.014019](https://doi.org/10.1103/PhysRevApplied.21.014019)

I. INTRODUCTION

In recent years, quantum computing has been a field of fast-growing interest and intense research. In the quest for a large-scale quantum computing architecture, individual processing units can be interconnected via a coherent mediator, allowing entanglement to be spread across the quantum circuit. Semiconductor spin qubits offer extended coherence times, compatibility with existing semiconductor technology, and the potential for scalability. While many different schemes for short-range nearest-neighbor entanglement of spin qubits have been demonstrated and perfected [1–4], long-range coupling of distant spin qubits remains a challenge. To date, some approaches to achieve long-range qubit entanglement include coherently shuttling electrons using gate-voltage pulses [5,6] or surface acoustic waves [7–10], coupling spin qubits with a much larger coupling quantum dot (QD) [11], or using a microwave cavity as a mediator [12–16].

Strong spin-photon coupling has been achieved in circuit quantum electrodynamics (cQED) device architectures by isolating a single electron in an Si double quantum dot (DQD) and utilizing the field gradient from a nearby micromagnet to engineer a synthetic spin-orbit interaction [12,13]. Exchange-only spin qubits fabricated

in GaAs have also reached the strong-coupling regime [14]. Resonant coupling of two spin qubits separated by approximately 4 μm has been demonstrated [15] and attempts have been made to extend cavity-mediated spin-spin coupling into the dispersive regime [17]. However, a larger spin-photon coupling rate, g_s , is needed to achieve high-fidelity remote gates between spatially separated spins.

The spin-photon coupling rate is set by the electric dipole moment of the electron trapped in the DQD, the cavity electric field, and the strength of the effective spin-orbit interaction. The cavity field is a function of the characteristic impedance of the resonator, Z_C . Therefore, an enhancement in g_s can be achieved by increasing Z_C , as $g_s \propto g_c \propto \sqrt{Z_C}$. The kinetic inductance can be greatly increased using large arrays of superconducting quantum interference devices (SQUIDs) [18]. However, for single spin qubits, the magnetic fields required to Zeeman split the spin states interferes with the operation of SQUID arrays.

Another way to increase the characteristic impedance of the resonator is to fabricate it from a high-kinetic-inductance superconducting film. The resonator impedance is given by $Z_C = \sqrt{L/C}$, where L and C are the characteristic inductance and capacitance. The inductance $L = L_m + L_k$, can be separated into magnetic, L_m , and kinetic, L_k , components. In past experiments, the magnetic inductance has been modestly increased using narrow

*petta@physics.ucla.edu

Nb strip-line resonators with an estimated impedance of $Z_C \sim 300 \Omega$ [12]. For some superconducting materials, L_k is dominant compared with L_m [19]. Therefore, to tune Z_C to a greater extent, high-kinetic-inductance materials are desirable. The prospect of larger coupling strengths has motivated investigations of many different high- L_k materials, including NbTiN [20,21], NbN [22,23], and TiN [24]. Since L_k is directly proportional to the ratio of the resonator length l to the cross-section area of the superconducting film [25], an effective approach is to fabricate a narrow resonator from a thin film of a high- L_k material [17,21].

In this paper, we study high- L_k NbN thin films and present two different approaches for extracting the sheet kinetic inductance $L_{k,S}$. We begin with dc resistivity measurements across the superconducting transition and compute $L_{k,S}$ over a large range of film thicknesses. We next characterize the microwave response of quarter-wavelength ($\lambda/4$) hanger-style resonators fabricated from NbN. To investigate the thickness dependence of $L_{k,S}$, we measure a variety of resonators, and from the extracted resonance frequencies we determine the kinetic inductance contribution to the total inductance. The kinetic inductance values $L_{k,S}$ extracted from dc and microwave measurements are in good agreement. Lastly, we utilize thin NbN films to fabricate compact LC filters that are compatible with QD-cQED devices. These filters feature up to 60 dB of attenuation near typical cavity resonance frequencies of $f_c = 8$ GHz and have a footprint that is significantly smaller than our previous design [12].

II. NIOBIUM NITRIDE FILM DEPOSITION AND dc RESISTIVITY MEASUREMENTS

We begin by characterizing the sheet resistance and critical temperature T_C of unpatterned superconducting NbN thin films using dc transport measurements. From the Bardeen-Cooper-Schrieffer (BCS) theory of

superconductivity, these quantities can be used to estimate the kinetic inductance [19,26].

We use an AJA dc-magnetron sputtering system with a high-purity Nb target to deposit the NbN films. Taking the critical temperature T_C as a metric, we optimize the deposition parameters, including the gas flow rates, target power, and deposition pressure. With a base pressure below 2×10^{-9} Torr, we initiate the deposition process by introducing N_2 and Ar into the system at flow rates of 6 sccm and 60 sccm to condition the chamber. We then bias the Nb target with a power of 400 W to ignite a plasma. The plasma of ions dislodges Nb atoms from the target and the Nb atoms react with N_2 to form NbN, which then deposits onto the substrate. The chamber pressure is held at 10 mTorr during deposition. We then deposit five NbN thin films of various thicknesses, with the substrate held at room temperature, utilizing a deposition rate of approximately 12 Å/s.

The thin films are characterized in a physical-property-measurement system (PPMS). We measure the sheet resistance R_\square as a function of the temperature T using conventional four-probe transport techniques. As shown in Fig. 1(a), all films exhibit sharp superconducting transitions below $T = 12$ K. From each cool-down curve, we extract the superconducting critical temperature T_C and the normal-state sheet resistance just before the superconducting transition R_\square^* . T_C is defined as the temperature at which R_\square drops to half of its normal-state value. T_C and R_\square^* are plotted as a function of the film thickness t in Fig. 1(b). As the film thickness t decreases, R_\square^* increases, while T_C monotonically decreases. The general trends observed in the temperature dependence of T_C and R_\square^* are in agreement with prior work on NbN [27–29] and align very well with the findings from similar materials [24]. In Fig. 1(c), we plot tT_C as a function of R_\square^* . The data are fitted to the scaling relation $tT_C = AR_\square^{*-b}$ [30]. We extract the exponent $b = 1.1 \pm 0.3$, which agrees with the value $b \approx 0.9 \sim 1.1$

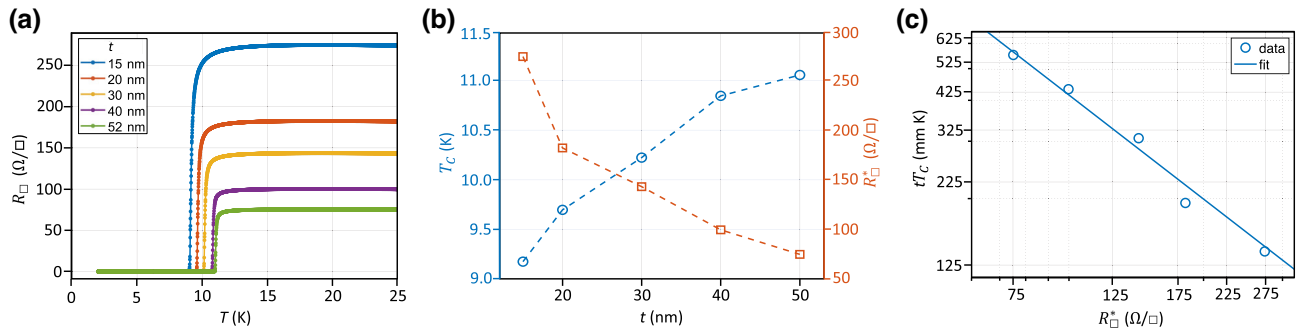


FIG. 1. (a) The temperature dependence of the sheet resistance R_\square for NbN thin films of different thicknesses t measured near the superconducting transition. (b) The critical temperature T_C and normal-state sheet resistance R_\square^* as a function of t . The dashed lines are guides to the eye. (c) tT_C plotted as a function of R_\square^* . The blue solid line is a fit to the universal scaling relation $tT_C = AR_\square^{*-b}$, yielding the power-law exponent $b = 1.1 \pm 0.3$.

TABLE I. The critical temperature T_C , the normal-state sheet resistance R_{\square}^* , and the sheet kinetic inductance $L_{k,S}$ for various film thicknesses t .

t (nm)	T_C (K)	R_{\square}^* (Ω/\square)	$L_{k,S}$ (pH/ \square)
15	9.2	273.9	41.2
20	9.7	182.1	25.9
30	10.2	143.2	19.3
40	10.8	99.8	12.7
52	11.1	75.1	9.4

that is widely observed in high-quality superconducting thin films [24,30,31].

Using the extracted T_C and R_{\square}^* , we estimate the sheet kinetic inductance using the formula [19]

$$L_{k,S} = \frac{\hbar R_{\square}^*}{\pi \Delta_0}, \quad (1)$$

where \hbar is the reduced Planck's constant and Δ_0 is the zero-temperature superconducting gap. Assuming that the NbN thin films obey BCS theory, $\Delta_0 = 1.76 \times k_B T_C$, where k_B is Boltzmann's constant [26]. The extracted values of T_C , R_{\square}^* , and the evaluated results of $L_{k,S}$ are given in Table I. As t decreases from 52 nm to 15 nm, we observe a large increase in R_{\square}^* from 75.1 Ω/\square to 273.9 Ω/\square and a small decrease in T_C from 11.1 K to 9.2 K, resulting in a significant increase in $L_{k,S}$ from 9.4 pH/ \square to 41.2 pH/ \square . These estimated kinetic inductance values allow for the efficient design of microwave cavities.

III. MICROWAVE-RESONATOR CHARACTERIZATION OF THE KINETIC INDUCTANCE

Using the kinetic inductance values obtained in Sec. II, we design microwave cavities with resonance frequencies ranging from 5.8 to 6.4 GHz. We fabricate an array of $\lambda/4$ cavities that are coupled to a transmission line. The side-coupled cavities allow for the efficient extraction of resonance frequencies and quality factors [25,32]. By fabricating resonators with different dimensions, we can quantitatively extract the magnetic and kinetic contributions to the total inductance.

As shown in Fig. 2(a), a typical resonator chip contains 12 $\lambda/4$ resonators of varying length l , each capacitively coupled to a central transmission line. The sample is made from a 30-nm NbN thin film sputtered on a high-resistivity Si substrate and the resonators are of the coplanar waveguide (CPW) design with a central conductor width of $a = 10 \mu\text{m}$ and a gap width of $s = 6.2 \mu\text{m}$. We use a network analyzer to characterize the microwave response of the sample, $|S_{21}(f)|$, in a dilution refrigerator with a lattice temperature of approximately 10 mK. Each resonance

results in a Lorentzian dip in $|S_{21}(f)|$. In Fig. 2(b), 12 resonances are observed (highlighted in red), corresponding to the 12 different resonator lengths.

In Fig. 2(c), we plot the extracted resonance frequencies of all 12 resonators and observe the expected relationship $f \propto 1/l$. For a $\lambda/4$ resonator, the resonator length can be written as

$$l = \lambda/4 = \frac{v_{\text{eff}}}{4f_0}, \quad (2)$$

where λ is the wavelength and f_0 is the resonance frequency. For nonmagnetic substrates, the propagation speed is $v_{\text{eff}} = c/\sqrt{\mu_{\text{eff}}\epsilon_{\text{eff}}} \approx c/\sqrt{\epsilon_{\text{eff}}}$, where c is the speed of light in vacuum, μ_{eff} is the relative magnetic permeability, and ϵ_{eff} is the relative dielectric constant, defined as

$$\epsilon_{\text{eff}} = \frac{1 + \epsilon_r \tilde{K}}{1 + \tilde{K}}. \quad (3)$$

The value of ϵ_{eff} is determined by the geometry of the CPW resonator and the relative dielectric constant of the substrate $\epsilon_r = 11.7$, with \tilde{K} given by

$$\tilde{K} = \frac{K(k')K(k_3)}{K(k)K(k'_3)}. \quad (4)$$

Here, K is the complete elliptical integral of the first kind, with $k = a/b$, $k_3 = \tanh(\pi a/4h)/\tanh(\pi b/4h)$, $k' = \sqrt{1 - k^2}$, $k'_3 = \sqrt{1 - k_3^2}$, and $b = a + 2s$, where a is the center-conductor width, s is the gap width, and h is the substrate thickness [33,34].

In a CPW geometry, the magnetic inductance per unit length is given by [32]:

$$L_m = \frac{\mu K(k')}{4 K(k)}, \quad (5)$$

where μ is the magnetic permeability of the substrate. In the case of a high- L_k resonator, the kinetic inductance must be included to obtain the total inductance, $L = L_m + L_k$. With $f \propto 1/\sqrt{L}$, we can fit to the data to extract $L_{k,S} = 20.9 \text{ pH}/\square$ [the solid line in Fig. 2(c)], which is close to the estimate obtained from the PPMS data. As the magnetic inductance only depends on the CPW geometry, we use the resonator dimensions to calculate the sheet magnetic inductance $L_{m,S} = 4.4 \text{ pH}/\square$.

To investigate the thickness dependence of $L_{k,S}$, we fabricate a variety of hanger-style resonators using NbN thin films of different thicknesses. For each film thickness, we determine $L_{k,S}$ by fitting to the measured resonance frequencies, as described in the previous paragraph. Figure 3 combines results from dc resistivity measurements and microwave-resonator characterization. The values of $L_{k,S}$ extracted from the microwave measurements are in good

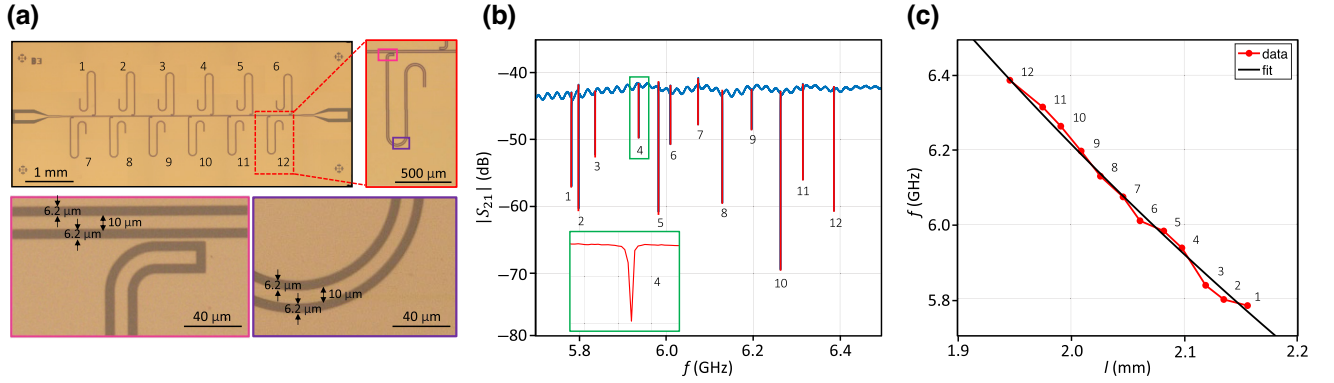


FIG. 2. The microwave characterization of hanger-style resonators. (a) Optical images of samples containing $12 \lambda/4$ resonators of varying length l that are coupled to a central transmission line. The insets feature enlarged images showing the resonator dimensions. (b) The microwave transmission $|S_{21}(f)|$ through a sample made from a 30-nm NbN film. The 12 resonances are highlighted in red. The inset shows an enlargement of $|S_{21}(f)|$ near the resonance at $f = 5.9$ GHz. (c) The extracted resonance frequencies plotted as a function of l , showing the expected $1/l$ dependence. A linear fit to the data (solid line) using a transmission line model yields a sheet kinetic inductance of $L_{k,S} = 20.9$ pH/ \square .

agreement with the estimates obtained from the dc transport measurements. The kinetic inductance of the NbN films is significant. For a direct comparison, the kinetic inductance extracted from a set of resonators fabricated on a conventional 50-nm-thick Nb film is only $L_{k,S} = 0.5$ pH/ \square .

As expected from theory, $L_{k,S}$ increases rapidly as t is reduced below 50 nm, with the highest value of $L_{k,S} = 58.7$ pH/ \square obtained from hanger resonators made from a 12.5-nm film. Our past cQED devices have utilized 50-nm Nb films and the largest coupling rates measured were $g_c \approx 58$ MHz in Ref. [16] and $g_{c(s)} \approx 40(11)$ MHz in Ref. [15]. To estimate the potential enhancement in $g_{c(s)}$ by switching to 15-nm NbN with $L_{k,S} = 41.2$ pH/ \square , we compare the

total inductances assuming the same $\lambda/2$ resonator design using the two different materials. The $\lambda/2$ resonators on our current QD-cQED chips have a center-pin width of $a = 0.75$ μm and a gap width of $s = 19.63$ μm , which yields a sheet magnetic inductance $L_{m,S} = 0.85$ pH/ \square . With 15-nm NbN thick films, the magnetic inductance is only 2% of the total inductance. Since $g_{c(s)} \propto \sqrt{Z_C} \propto L^{1/4}$, switching from 50-nm Nb to 15-nm NbN is expected to result in a $5.6\times$ increase in Z_C and hence a $2.4\times$ increase in $g_{c(s)}$.

IV. LC MICROWAVE FILTERS FOR QUANTUM DOT CIRCUIT QUANTUM ELECTRODYNAMICS

We now utilize high-kinetic-inductance NbN films to fabricate compact microwave filters. Measurements of early QD-cQED devices show significant microwave leakage through the wiring used to dc bias the QD gate electrodes [35]. The resulting photon-leakage pathways can lower the cavity quality factor significantly. To suppress photon leakage, on-chip low-pass LC filters are often connected in series with each gate line [36]. A prior work that focuses on on-chip filters for high impedance resonators in QD-cQED device platforms demonstrates a filter design consisting of a nanowire inductor and a thin-film capacitor [21]. The overlapping thin-film capacitor is compact but requires additional steps in fabrication. Considering the specific requirements of quantum dot devices, where fewer fabrication steps can lead to better hygiene, improved reliability, and potentially enhanced device performance, we opt for a planar LC-filter design, comprising a spiral inductor and an interdigitated capacitor (see the insets to Fig. 4), both of which are patterned from the same high- L_k film as the resonator. We simulate different designs using the

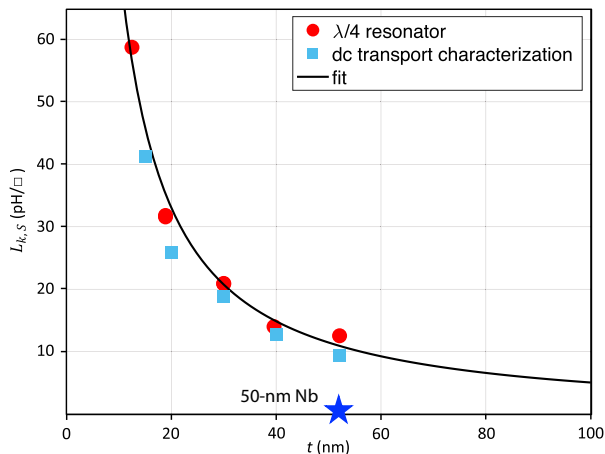


FIG. 3. The thickness dependence of the sheet kinetic inductance $L_{k,S}$. The data are extracted from the dc characterization of the thin-film resistivity (Sec. II) and the microwave response of $\lambda/4$ resonators (Sec. III). The blue star indicates the much smaller $L_{k,S} = 0.5$ pH/ \square of a standard 50-nm Nb film.

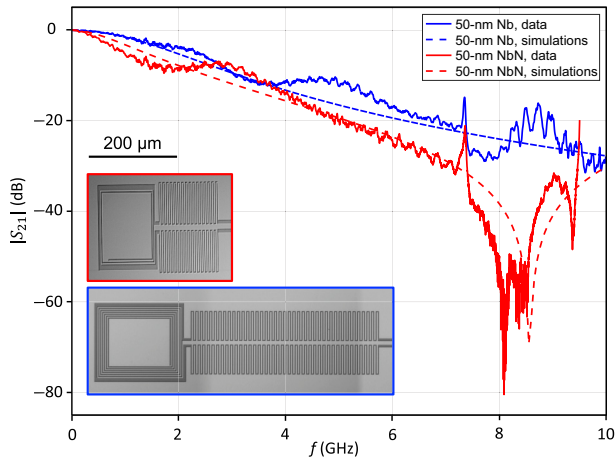


FIG. 4. Measurements of $|S_{21}(f)|$ for two LC filters (solid lines) and the simulated response (dashed lines). The 15-nm NbN filter (red) gives a substantial attenuation of 60 dB around 8 GHz. In comparison, we measure 24 dB of attenuation using an approximately $2\times$ longer filter made from a 50-nm Nb film (blue). The insets show optical images of filters fabricated from a 15-nm NbN film (outlined in red) and a 50-nm Nb film (outlined in blue).

SONNET EM simulation package and fabricate Nb and NbN filters to evaluate their performance.

Figure 4 shows the microwave transmission $|S_{21}(f)|$ through two types of filters that are cooled to $T \sim 700$ mK. The filter fabricated from a standard 50-nm-thick Nb film provides approximately 24 dB of attenuation near a typical cavity frequency of 8 GHz [36]. In contrast, a filter fabricated using a 15-nm-thick NbN film is approximately $2\times$ shorter and provides a much larger attenuation of 60 dB near 8 GHz. The experimental data are in good agreement with the SONNET simulations. These measurements show that the utilization of NbN films can significantly reduce the filter sizes and provide a higher degree of attenuation to reduce the cavity losses.

V. CONCLUSIONS

In summary, we have investigated the thickness dependence of the sheet kinetic inductance of sputtered NbN thin films using a combination of dc transport and microwave measurements. To mitigate microwave leakage through the QD dc gate lines, we have tested different LC -filter designs and demonstrated 60 dB of attenuation near typical cavity resonance frequencies. Owing to the high L_k of NbN, we can now achieve much stronger on-chip filtering with a smaller filter footprint. The high kinetic inductance $L_{k,S} = 41.2$ pH/ \square of the 15 nm NbN film provides an opportunity to strongly enhance g_c and g_s , thereby moving QD-cQED systems further into the strong-coupling regime.

ACKNOWLEDGMENTS

This work was supported by Army Research Office Grants No. W911NF-15-1-0149 and No. W911NF-23-1-0104. The devices were fabricated in the Princeton University Quantum Device Nanofabrication Laboratory and in part in the Singh Center for Nanotechnology, which is supported by the National Science Foundation (NSF) National Nanotechnology Coordinated Infrastructure Program under Grant No. NNCI-2025608. N.P.O. acknowledges support from the U.S. Department of Energy (Grant No. DE-SC0017863).

- [1] J. R. Petta, A. C. Johnson, J. M. Taylor, E. A. Laird, A. Yacoby, M. D. Lukin, C. M. Marcus, M. P. Hanson, and A. C. Gossard, Coherent manipulation of coupled electron spins in semiconductor quantum dots, *Science* **309**, 2180 (2005).
- [2] P.-A. Mortemousque, E. Chanrion, B. Jadot, H. Flentje, A. Ludwig, A. D. Wieck, M. Urdampilleta, C. Bäuerle, and T. Meunier, Coherent control of individual electron spins in a two-dimensional quantum dot array, *Nat. Nanotechnol.* **16**, 296 (2021).
- [3] T. Watson, S. Philips, E. Kawakami, D. Ward, P. Scarlino, M. Veldhorst, D. Savage, M. Lagally, M. Friesen, and S. Coppersmith, *et al.*, A programmable two-qubit quantum processor in silicon, *Nature* **555**, 633 (2018).
- [4] D. Zajac, A. Sigillito, M. Russ, F. Borjans, J. Taylor, G. Burkard, and J. Petta, Resonantly driven CNOT gate for electron spins, *Science* **359**, 439 (2018).
- [5] T. A. Baart, M. Shafiei, T. Fujita, C. Reichl, W. Wegscheider, and L. M. K. Vandersypen, Single-spin charge-coupled device, *Nat. Nanotechnol.* **11**, 330 (2016).
- [6] A. Mills, D. Zajac, M. Gullans, F. Schupp, T. Hazard, and J. Petta, Shuttling a single charge across a one-dimensional array of silicon quantum dots, *Nat. Commun.* **10**, 1 (2019).
- [7] M. M. de Lima and P. V. Santos, Modulation of photonic structures by surface acoustic waves, *Rep. Prog. Phys.* **68**, 1639 (2005).
- [8] J. A. Stotz, R. Hey, P. V. Santos, and K. H. Ploog, Coherent spin transport through dynamic quantum dots, *Nat. Mater.* **4**, 585 (2005).
- [9] S. Hermelin, S. Takada, M. Yamamoto, S. Tarucha, A. D. Wieck, L. Saminadayar, C. Bäuerle, and T. Meunier, Electrons surfing on a sound wave as a platform for quantum optics with flying electrons, *Nature* **477**, 435 (2011).
- [10] R. McNeil, M. Kataoka, C. Ford, C. Barnes, D. Anderson, G. Jones, I. Farrer, and D. Ritchie, On-demand single-electron transfer between distant quantum dots, *Nature* **477**, 439 (2011).
- [11] F. K. Malinowski, F. Martins, T. B. Smith, S. D. Bartlett, A. C. Doherty, P. D. Nissen, S. Fallahi, G. C. Gardner, M. J. Manfra, and C. M. Marcus, *et al.*, Fast spin exchange across a multielectron mediator, *Nat. Commun.* **10**, 1 (2019).
- [12] X. Mi, M. Benito, S. Putz, D. M. Zajac, J. M. Taylor, G. Burkard, and J. R. Petta, A coherent spin-photon interface in silicon, *Nature* **555**, 599 (2018).

- [13] N. Samkharadze, G. Zheng, N. Kalhor, D. Brousse, A. Sammak, U. Mendes, A. Blais, G. Scappucci, and L. Vandersypen, Strong spin-photon coupling in silicon, *Science* **359**, 1123 (2018).
- [14] A. J. Landig, J. V. Koski, P. Scarlino, U. Mendes, A. Blais, C. Reichl, W. Wegscheider, A. Wallraff, K. Ensslin, and T. Ihn, Coherent spin-photon coupling using a resonant exchange qubit, *Nature* **560**, 179 (2018).
- [15] F. Borjans, X. Croot, X. Mi, M. Gullans, and J. Petta, Resonant microwave-mediated interactions between distant electron spins, *Nature* **577**, 195 (2020).
- [16] F. Borjans, X. Croot, S. Putz, X. Mi, S. Quinn, A. Pan, J. Kerckhoff, E. Pritchett, C. Jackson, and L. Edge, *et al.*, Split-gate cavity coupler for silicon circuit quantum electrodynamics, *Appl. Phys. Lett.* **116**, 234001 (2020).
- [17] P. Harvey-Collard, J. Dijkema, G. Zheng, A. Sammak, G. Scappucci, and L. M. Vandersypen, Coherent spin-spin coupling mediated by virtual microwave photons, *Phys. Rev. X* **12**, 021026 (2022).
- [18] A. Stockklauser, P. Scarlino, J. V. Koski, S. Gasparinetti, C. K. Andersen, C. Reichl, W. Wegscheider, T. Ihn, K. Ensslin, and A. Wallraff, Strong coupling cavity QED with gate-defined double quantum dots enabled by a high impedance resonator, *Phys. Rev. X* **7**, 011030 (2017).
- [19] J. Zmuidzinas, Superconducting microresonators: Physics and applications, *Annu. Rev. Condens. Matter Phys.* **3**, 169 (2012).
- [20] N. Samkharadze, A. Bruno, P. Scarlino, G. Zheng, D. P. DiVincenzo, L. DiCarlo, and L. M. K. Vandersypen, High-kinetic-inductance superconducting nanowire resonators for circuit QED in a magnetic field, *Phys. Rev. Appl.* **5**, 044004 (2016).
- [21] P. Harvey-Collard, G. Zheng, J. Dijkema, N. Samkharadze, A. Sammak, G. Scappucci, and L. M. Vandersypen, On-chip microwave filters for high-impedance resonators with gate-defined quantum dots, *Phys. Rev. Appl.* **14**, 034025 (2020).
- [22] D. Niepce, J. Burnett, and J. Bylander, High kinetic inductance NbN nanowire superinductors, *Phys. Rev. Appl.* **11**, 044014 (2019).
- [23] C. X. Yu, S. Zihlmann, G. Troncoso Fernandez-Bada, J.-L. Thomassin, F. Gustavo, E. Dumur, and R. Maurand, Magnetic field resilient high kinetic inductance superconducting niobium nitride coplanar waveguide resonators, *Appl. Phys. Lett.* **118**, 054001 (2021).
- [24] K. R. Amin, C. Ladner, G. Jourdan, S. Hentz, N. Roch, and J. Renard, Loss mechanisms in TiN high impedance superconducting microwave circuits, *Appl. Phys. Lett.* **120**, 164001 (2022).
- [25] M. Tinkham, *Introduction to Superconductivity* (Courier Corporation, North Chelmsford, MA, 2004).
- [26] J. Bardeen, L. N. Cooper, and J. R. Schrieffer, Theory of superconductivity, *Phys. Rev.* **108**, 1175 (1957).
- [27] S. Chockalingam, M. Chand, J. Jesudasan, V. Tripathi, and P. Raychaudhuri, Superconducting properties and Hall effect of epitaxial NbN thin films, *Phys. Rev. B* **77**, 214503 (2008).
- [28] D. Hazra, N. Tsavdaris, S. Jebari, A. Grimm, F. Blanchet, F. Mercier, E. Blanquet, C. Chapelier, and M. Hofheinz, Superconducting properties of very high quality NbN thin films grown by high temperature chemical vapor deposition, *Supercond. Sci. Technol.* **29**, 105011 (2016).
- [29] M. Shibalov, A. Mumlyakov, I. Trofimov, E. Timofeeva, A. Sirotina, E. Pershina, A. Tagachenkov, Y. Anufriev, E. Zenova, and N. Porokhov, *et al.*, Multistep atomic layer deposition process for ultrathin superconducting NbN films with high critical current density on amorphous substrate, *Supercond. Sci. Technol.* **34**, 085016 (2021).
- [30] Y. Ivry, C.-S. Kim, A. E. Dane, D. De Fazio, A. N. McCaughan, K. A. Sunter, Q. Zhao, and K. K. Berggren, Universal scaling of the critical temperature for thin films near the superconducting-to-insulating transition, *Phys. Rev. B* **90**, 214515 (2014).
- [31] M. Faverzani, E. Ferri, A. Giachero, C. Giordano, B. Margesin, R. Mezzena, A. Nucciotti, and A. Puiu, Characterization of the low temperature behavior of thin titanium/titanium nitride multilayer films, *Supercond. Sci. Technol.* **33**, 045009 (2020).
- [32] K. Yoshida, K. Watanabe, T. Kisu, and K. Enpuku, Evaluation of magnetic penetration depth and surface resistance of superconducting thin films using coplanar waveguides, *IEEE Trans. Appl. Supercond.* **5**, 1979 (1995).
- [33] D. I. Schuster, Ph.D. thesis, Graduate School, Yale University, https://rsl.yale.edu/sites/default/files/files/RSL_Theses/SchusterThesis.pdf (2007).
- [34] X. Mi, Ph.D. thesis, Graduate School, Princeton University, <http://arks.princeton.edu/ark:/88435/dsp019880vt68b> (2018).
- [35] K. D. Petersson, L. W. McFaul, M. D. Schroer, M. Jung, J. M. Taylor, A. A. Houck, and J. R. Petta, Circuit quantum electrodynamics with a spin qubit, *Nature* **490**, 380 (2012).
- [36] X. Mi, J. Cady, D. Zajac, J. Stehlik, L. Edge, and J. R. Petta, Circuit quantum electrodynamics architecture for gate-defined quantum dots in silicon, *Appl. Phys. Lett.* **110**, 043502 (2017).